

Neural Semantic Surface Maps

Luca Morreale¹  and Noam Aigerman^{2,3}  and Vladimir G. Kim³  and Niloy J. Mitra^{1,3} 

¹University College London

²University of Montreal

³Adobe Research



Figure 1: We propose an automatic method to produce a semantic map between a pair of upright-oriented surfaces. First, we aggregate a set of fuzzy and possibly erroneous correspondences obtained by lifting 2D semantic matches from a pre-trained vision transformer-based mapper and then use a novel formulation to distill out a coherent map. We do not use any geometric features, assume access to any form of ground truth maps, or restrict to isometric maps. Here, we show extracted maps between two non-isometric shapes (tiger and iguana). Though the genus zero surfaces are automatically cut to yield disc topologies, the extracted map, by construction, is seamless.

Abstract

We present an automated technique for computing a map between two genus-zero shapes, which matches semantically corresponding regions to one another. Lack of annotated data prohibits direct inference of 3D semantic priors; instead, current State-of-the-art methods predominantly optimize geometric properties or require varying amounts of manual annotation. To overcome the lack of annotated training data, we distill semantic matches from pre-trained vision models: our method renders the pair of 3D shapes from multiple viewpoints; the resulting renders are then fed into an off-the-shelf image-matching method which leverages a pretrained visual model to produce feature points. This yields semantic correspondences, which can be projected back to the 3D shapes, producing a raw matching that is inaccurate and inconsistent between different viewpoints. These correspondences are refined and distilled into an inter-surface map by a dedicated optimization scheme, which promotes bijectivity and continuity of the output map. We illustrate that our approach can generate semantic surface-to-surface maps, eliminating manual annotations or any 3D training data requirement. Furthermore, it proves effective in scenarios with high semantic complexity, where objects are non-isometrically related, as well as in situations where they are nearly isometric.

1. Introduction

In this work, we define an automatic method to compute a continuous correspondence between two surfaces, represented as meshes. Our core contribution is devising an approach for computing a *semantic* map that matches semantically corresponding points to one another (e.g., nose to nose, arm to arm).

Computing correspondences between domains is a fundamental and highly-researched problem, spanning a wide array of domains such as images [MJF*21], text snippets [HDT19], audio [ZLW*20], or general graphs [SZF20]. In the context of 3D surfaces, establishing such correspondences enables texture or deformation transfer [SP04,BVGP09], shape analysis [TP91,BRPM*16,

BRLB14a, PWH*15], and shape space exploration [HWAG09, MCA*22, YYPM11].

Continuous surfaces (2-manifolds), encoded as triangular meshes, remain the most natural and common representation of 3D shapes in graphics and discrete differential geometry. Correspondence between two such surfaces is typically required to be a map that is continuous, one-to-one, onto, and with a continuous inverse, *i.e.*, a *homeomorphism*. Decades of research (see surveys [Sah20, EST*19]) have been dedicated to tackle the task of mapping between surface pairs. These previous works cannot extract (semantic) maps over the space of homeomorphisms; instead, they have focused on surrogate optimization tasks that minimize some geometric notion of “distortion” of the map, *e.g.*, preserving geodesic distances as best as possible. Such distortion-minimizing geometrically-guided maps are, of course, not necessarily semantically meaningful. Thus, a human-in-the-loop approach is usually taken to manually indicate landmark correspondences, which are then used to optimize a map.

Computing semantic homeomorphism faces two main challenges. First, the lack of annotated 3D data inhibits learning high-level semantic priors. In contrast, considering the image domain, recent works [SPV*21, HZH*22, VHVZ22, AGBD21, ODM*23] demonstrate that the features of a pre-trained vision transformer (ViT) are often semantically meaningful and can be used reliably across multiple vision tasks, even on out-of-training image data in a zero-shot setting. Second, most 3D representations either hinder or - completely - prevent the computation of bijective inter-surface maps from semantic priors. We aim to bridge the semantic matching capabilities of the image domain with the computation of inter-surface maps from potentially noisy correspondences, encouraging continuity and bijectivity. Our core observation is that suitable renderings of the surfaces, without access to surface texture, are already sufficient for image transformers (*i.e.*, ViT) to produce 2D matches that can subsequently be used as fuzzy (*i.e.*, partial and non-injective) maps between the surfaces. Then, we formulate an optimization to aggregate multiple such fuzzy matches obtained from multiview renderings to produce a surface map that best conforms to these fuzzy matches, thereby distilling their semantic priors, Figure 1.

Specifically, given the fuzzy matches, we utilize Neural Surface Maps (NSM) [MAKM21] to optimize a map between two surfaces. The original NSM framework encodes surfaces using dedicated neural functions, offering a differentiable backbone and avoiding complexities arising from topological changes (*i.e.*, mesh connectivity for different triangulations). However, it has two limitations: it expects the individual surfaces to be cut into disc topologies with the two respective boundaries *already* in correspondence and requires a set of exact landmark correspondences. We address the first problem by proposing a seamless Neural Surface Maps (sNSM) framework, which relaxes the requirement from exact boundary correspondences to only cone-point matchings. We address the second problem by optimizing a custom objective that encourages the image of a specific point to best accommodate the fuzzy (semantic) matches while identifying and disregarding outliers (see Figure 2). The resultant optimization problem is solved using gradient descent, simply through PyTorch’s SGD optimizer.

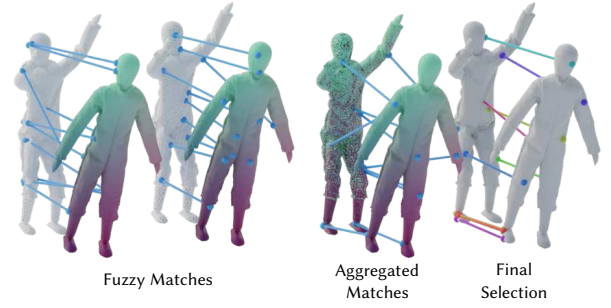


Figure 2: ViT-based semantic correspondences. (Left) We lift 2D image-based correspondences, obtained using a pre-trained vision-transformer [ODM*23] on rendered image source/target pairs from sampled views, to obtain fuzzy and spurious 3D (semantic) correspondences. We collect correspondence (shown with coloring and a random set highlighted with lines) from each of the sampled views and aggregate them across views to get fuzzy matches (middle), which contain erroneous matching (*e.g.*, thigh getting mapped to the arm). (Right) We propose an optimization to distill these fuzzy matches into an inter-surface map.

Through quantitative and qualitative experiments, we evaluate our ability to match upright object pairs with varying levels of isometry for objects from the same semantic class and across different ones. We also compare ours to competing surface map extraction algorithms. In summary, our main contributions are:

- proposing a fully automatic algorithm for extracting semantic maps between upright shape pairs;
- sampling and integrating a set of image-based correspondences to form fuzzy object space correspondence maps;
- proposing a sNSM framework that can work with fuzzy, and potentially noisy guidance, to distill semantic maps; and
- demonstrating, via extensive evaluation and comparisons, that the algorithm yields semantically valid maps for both isometrically and non-isometrically related shape pairs.

2. Related Works

2.1. Shape matching

Shape matching and correspondence estimation have been widely studied in geometry processing. In the most straightforward setting where rigid transforms relate shape pairs, iterative closest points methods [RL01, ZSN03] are often used, followed by refinement using deep learned features to identify good correspondences to improve the initial alignment [GZWW19, DBI18, WS19]. Directly optimizing for distance preservation is computationally challenging for surfaces [BBK06, HAWG08] discretized as dense triangulations. Optimal transport has been used to optimize over relatively coarse shape representations [SPKS16].

Functional maps compute a fuzzy correspondence by aligning the spectral basis of two shapes that are related by linear transforms for near-isometric deformations [OBSC*12, CSBC*17]. The approach offers an elegant machinery to compute shape correspondence and has been extended to handle partial matching [LRB*18], learning spectral alignment [LRR*17, DSO20], finding multiple

low-distortion maps [RMOW20], and leveraging optimal transport methods [PRM*21] (c.f. course notes [OCB*17] for other variations). While variants have been proposed to ‘project’ functional maps to point-to-point maps, such approaches [EBC17] do not explicitly ensure the bijectivity of the maps.

Restricting optimizations directly to surfaces poses a challenge since the most common surface representation, a triangle mesh, does not easily lend itself to continuous optimization. Schreiner *et al.* [SAPH04] optimize surface-to-surface maps via direct mesh-mesh intersection, which leads to a combinatorial problem due to the surface discretization into triangles. Subsequent approaches represent maps by parameterizing meshes to a common domain such as a plane [APL14, SBCK19] or a sphere [APH05, SPK23], which can give a bijective final map, but still does not offer a natural way to optimize using inter-surface distortion. Notably, Schmidt *et al.* [SPK23] propose a coarse-to-fine optimization strategy, defined between spheres, that uses incremental re-meshing to significantly speed up the optimization and improve the quality of the map, yet relies on few manual annotations.

Others treated inter-surface mapping as a problem of exploring a space of low-distortion maps, for example, blending across conformal maps Blended Intrinsic Maps (BIM) [KLF11] were explored and interpolated. Recent work by Edelstein *et al.* [EEBC20] proposed Enigma, leveraging genetic algorithms, to achieve state-of-the-art results. In MapTree [RMOW20], authors explore multiple functional maps between near-isometric shape pairs. They propose a fully automatic method that reveals multiple and diverse maps by first enumerating map variations and then optimizing them to extract dense pointwise maps.

Parallel to this work, Abdelreheem *et al.* [AEOW23] proposed a pipeline to extract coarse correspondences between shapes through pre-trained networks. In particular, the authors use [LLSH23] to extract a shape class description, *e.g.*, human or person; such class is then used to extract semantic descriptions for shape subparts, *e.g.*, leg or arm. Finally, SAM [KMR*23] extracts features based on these keywords and renderings to extract features for each shape. The resulting features are then used for co-shape segmentation and shape correspondences. The latter is achieved through the functional map framework, [RPWO18], which natively produces a fuzzy map, and thus may not reduce, or refine, the fuzziness of the initial set of correspondences.

Instead of functional maps, which assumes there exists a linear spectral map and is less suitable for optimizing for bijectivity, our work builds on NSM [MAKM21] that maps shapes through common 2D domains. However, the original technique implicitly assumes shapes to have corresponding boundaries, making it unsuitable for fully automatic mapping. Thus, we modify the formulation to be seamless around the boundary to allow for arbitrary non-matching cuts on different surfaces. We rely only on DinoV2 [ODM*23] to extract features from shape renderings, allowing us to leverage point-level (rather than part-level) correspondence priors.

2.2. Image-based shape analysis

Image-based representations are commonly used for 3D shape analysis tasks, such as classification [SMKL15], segmentation [SYM*22, KYF*20, DLH22], or matching [HKC*17], where a shape is first rendered from multiple viewpoints, the resulting images are analyzed with 2D neural networks, and then the output is aggregated on the 3D shape via additional optimization [KAMC17]. While these methods often start with pre-trained 2D neural networks, they all require additional fine-tuning with 3D supervision and thus can only work on categories of shapes with labeled 3D data. Indeed, Genova *et al.* [GYK*21], train a 3D segmentation technique by using a 2D method to produce pseudo labels. Recently, [ASOW23] describes a training-free approach for 3D shape semantic segmentation through the use of pre-trained visual transformers. Our approach exploits a similar intuition to extract semantic shape correspondences, to then distill an inter-surface map from them, thus *without* any 3D supervision.

2.3. Visual features

The use of pre-trained CNNs features marked an important milestone for computer vision tasks, such as object detection and segmentation [GDDM14], or image synthesis [GEB16, SGM*20]. These network representations encode a wide range of visual information from low-level (statistical) features, (*e.g.*, edges, auto-correlation matrices, color, to high-level semantic features), object parts, and structure [OMS17, CAS*19, MGY*19]. However, these methods [LLUZ16] usually are restricted to local (CNN) neighborhoods or pre-authored nonlocal receptive field, and ignore long-range dependencies [WGGH18].

Vision Transformers [DBK*20], dubbed ViT, belong to a family of recent and powerful neural architecture that can discover both local and nonlocal relations. A noteworthy example is DINO-ViT [CTM*21] that trains a transformer network through self-distillation and uses its features in several tasks, *e.g.*, image retrieval and object segmentation. Several works demonstrated the utility of Dino-ViT internal representation as a black box [SPV*21, WSH*22] for tasks such as semantic segmentation [HZH*22] and category discovery [VHVZ22]. Amir *et al.* [AGBD21] study in depth these features and use them to solve vision tasks, such as image correspondences, in zero-shot settings. Recently, Oquab *et al.* [ODM*23] extended Dino-ViT, introducing Dinov2, showcasing enhanced and more coherent feature semantic interpretability compared to the original version, and also exhibiting broader applicability.

3. Method

We now detail our framework (see Figure 3). We assume to be given two upright 3D surfaces, **A** and **B**, in arbitrary relative poses. Although the method can be extended to handle any genus surfaces, we assume both shapes to have zero genus. We aim to compute an inter-surface map $\Psi : \mathbf{A} \leftrightarrow \mathbf{B}$ guided by visual semantics. Our framework proceeds in three stages:

- (i) Given two shapes, **A** and **B**, that are assumed to be oriented upright, we automatically align them using semantic matches.

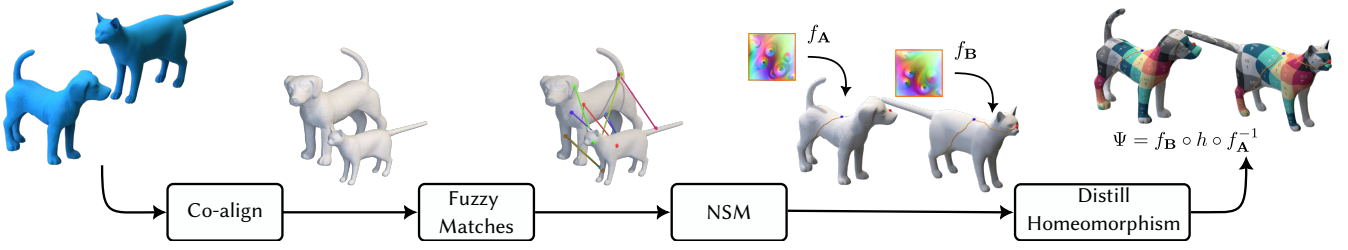


Figure 3: Overview. Starting from a pair of upright surfaces, we automatically distill an inter-surface map from a set of fuzzy matches. First, we align the input shapes, then extract a set of fuzzy matches through DinoV2 [ODM*23] semantic visual features. We use these features to first independently cut the two meshes and then optimize a (seamless) map between them.

- (ii) We aggregate fuzzy matches (i.e., general matching of pairs of points which is neither 1-to-1, onto, nor maps all points on the source surface) between the surfaces by applying 2D matching techniques to renderings, over multiple views.
- (iii) Optimize a surface map that best agrees with the fuzzy semantic matches while handling outliers.

3.1. Semantic Shape Alignment

Given two upright shapes, **A** and **B**, we first align them to have the same orientations. We achieve this by casting this problem as (semantic) circular string matching between shape renderings: given two ‘strings’ - sets of renderings - of the same length, we find the global rotation **R** to best align one string with the other. Intuitively, we order one sequence to convey semantic information in the same order as the other, see Figure 4 for an overview.

First, we render each mesh from 12 viewpoints around it, R_i^A and R_i^B (see Subsection 3.4 for a discussion on rendering). These images constitute the two strings $s^A = \{R_i^A\}$ and $s^B = \{R_i^B\}$. Then, we extract a set of features with DinoV2 [ODM*23] for each image. Finally, we compute the alignment score for the 12 possible rotations as the total number of “Best Buddy matches” [DOR*15] between the two strings of features. We pick the (relative) rotation with the highest score as the rotation and use it to align the shape pairs.

3.2. Distilling Fuzzy 3D Matches via Visual Semantics

Next, we extract fuzzy matches from renderings, taken from different viewpoints, of the aligned surfaces. Each such viewpoint V results in a pair of rendering that we use to define a fuzzy correspondence $\phi^V := (p_i^V, q_i^V)_{i=1}^n$ with $p \in A, q \in B$, which consists of pairs of corresponding points on **A** and **B**.

3.2.1. Computing rendering correspondences

Given a viewpoint V , we render the two surfaces from that viewpoint to get two renderings, R_V^A and R_V^B . To extract correspondences, we take inspiration from recent methods that leverage deep image features from [ODM*23] for matching 2D images and design a method for extracting dense visual correspondences. Specifically, we extract patch features with λ_i^A and λ_i^B being the features

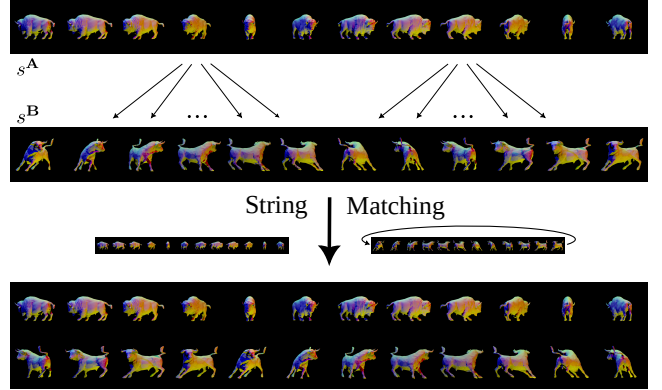


Figure 4: Co-aligning input surfaces: Starting from a pair of upright meshes (bison and bull in this example), we render 12 views around them (s^A and s^B). Then, we extract DinoV2 features from each rendering independently and match these features as a string-matching problem. Specifically, we optimize over a cyclic shift of the rendered views (i.e., one degree of freedom) to maximize agreement of image-based semantic correspondences.

of rendering of R_V^A and R_V^B , respectively. Then, we segment foreground/background through PCA and compute the cosine similarity between all pairs of source and target patch foreground features, as score

$$S_{ij} = \langle \lambda_i^A, \lambda_j^B \rangle. \quad (1)$$

Finally, we define the match of patch $i \in R_V^A$ as the patch $j \in R_V^B$ with the highest cosine similarity, and vice versa, the match of patch $j \in R_V^B$ as the patch $i \in R_V^A$ with the highest cosine similarity. In summary, the pair $(i, j), i \in R_V^A, j \in R_V^B$ is a match, if

$$S_{ij} = \max_k S_{ik} \text{ or } S_{ij} = \max_l S_{lj}. \quad (2)$$

We transform a match from patch level to pixel level, as the patch size is known. Note that in contrast to us, [AGBD21] selects only “Best Buddy” matches [DOR*15], augment features with binning, and does not segment foreground/background through PCA features. Although [AGBD21] produces a more expressive set of features, and possibly a more reliable set of fuzzy matches, it is extremely time-consuming, and our experiments did not provide sufficient justification for such a design choice.

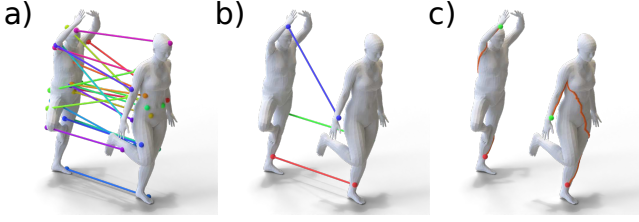


Figure 5: Cutting through cone points. We collect a set of spurious and noisy matches (a). Then, we select the more reliable $K = 3$ correspondence (b). Finally, using these matches as cut endpoints, or cones, we cut the two meshes independently (c). Note how the cut differs in the two shapes: the man is cut through the back, while the woman is cut through the front.

Given dense 2D correspondences in an image, we lift (unproject) each pixel to the 3D mesh by performing ray intersection between that pixel’s corresponding ray from viewpoint V and the 3D mesh \mathbf{T} , thereby associating every 2D pixel with a point on the surface, represented as barycentric coordinates at the triangle the ray intersects. The fuzzy matches are thus pairs of matching 3D points (represented as barycentric coordinates on triangles): $(\phi^V = p_i, q_i)_{i=1}^n$.

We repeat this process from multiple viewpoints and obtain a collection $\{\phi^i\}_{i=1}^k$ of fuzzy matches. Our final task is to distill them to produce a map.

3.3. Aggregating the Fuzzy Matches to an Inter-surface map

Given the fuzzy matches, we wish to optimize a continuous map Ψ between \mathbf{A} and \mathbf{B} using a differentiable loss that encourages agreement with the fuzzy matches.

Our final goal is thus to devise an optimization scheme that will lead to a map $\Psi : \mathbf{A} \leftrightarrow \mathbf{B}$ which agrees with as many matches as possible, provided by the different fuzzy matches. To achieve this goal, we compare each point’s image with its designated matches from ϕ^i . We then use an L_1 norm over the error of different points, which is known to be robust to outliers and encourage sparsity (i.e., agree with as many matches of the fuzzy matches as possible) as:

$$\mathcal{L}_{\text{matches}} = \min \sum_{i,j} \frac{1}{|\phi^i|} \|\Psi(p_j) - q_j\|_1 \quad (3)$$

where (p_j, q_j) are the j matching pair in ϕ^i , and $|\phi^i|$ is the number of matches in ϕ^i .

To optimize (3), we adopt a recent method for optimization of surface map, Neural Surface Maps (NSM) [MAKM21] as described next.

3.3.1. Seamless Neural Surface Map

We follow NSM’s paradigm: we first parameterize each one of the two cut surfaces via SLIM [RPPSH17] into a square $D \in \mathbb{R}^2$ to get two bijective seamless parameterizations, $P_{\mathbf{A}} : \mathbf{A} \leftrightarrow D, P_{\mathbf{B}} : \mathbf{B} \leftrightarrow D$. Then, we fit a neural network to each of the two parameterizations’ inverse, $f_{\mathbf{A}} \approx P_{\mathbf{A}}^{-1}, f_{\mathbf{B}} \approx P_{\mathbf{B}}^{-1}$. Finally, using another neural network that maps the square to itself, h , we can define the inter-surface map $\Psi = f_{\mathbf{B}} \circ h \circ f_{\mathbf{A}}^{-1}$. By optimizing solely the parameters

of h while maintaining its bijectivity, and holding the overfitted networks $f_{\mathbf{A}}, f_{\mathbf{B}}$ fixed, NSM enables us to optimize over the space of maps between the two surfaces.

As we cannot guarantee corresponding cuts between genus 0 meshes, see cut examples in Figure 5, we relax the boundary-matching constraint in the original NSM and extend it to support seamless maps. Intuitively, a borderless, or seamless, parameterization is a 2D-3D mapping that is independent of the choice of cut path, given a set of K boundary points. In other words, the map emerging from the parametrization has several equivalent maps with different boundaries, see Figure 6(c). Only the K points, referred to as cones, remain constant and must have the same mapping across all equivalent maps. Mathematically, a seamless parametrization is a mapping equipped with homotopic cuts (i.e., the cuts can be changed homotopically but the produced mapping will stay the same). In particular, for three cones on a sphere, all cuts are homotopic, and thus the embedding is independent of the cut choice. Please refer to [APL15] for more details.

Furthermore, the class of seamless parametrization requires a specific type of cut such that triangles, or points for that matter, can be mapped to the other side of the cut by a family of transformations \mathcal{R} . In terms of NSM, a seamless map requires matching corresponding cones while the boundary is allowed to move. Thus, the accuracy required to define the cut path, and hence the 2D boundary, through fuzzy matches is reduced, e.g., see Figure 5(c) for cut paths. Below, we first detail how we extract corresponding cones, then describe a seamless map.

3.3.2. Cones

To identify cones, we first aggregate the fuzzy matches by counting for each triangle $F_i^{\mathbf{A}} \in \mathbf{A}$, how many fuzzy matches associate it with triangle $F_j^{\mathbf{B}} \in \mathbf{B}$, yielding a large sparse matrix M such that its (i, j) entry is the total count for matches of $F_i^{\mathbf{A}}$ to $F_j^{\mathbf{B}}$,

$$M_{ij} = \sum_k \left| \left\{ (p, q) \text{ s.t. } p \in F_i^{\mathbf{A}}, q \in F_j^{\mathbf{B}}, (p, q) \in \phi^k \right\} \right|, \quad (4)$$

where $|\cdot|$ stands for the cardinality of the set. Next, we consider M as the adjacency matrix of an edge-weighted graph, with M_{ij} being the weight on edge (i, j) . Then, through bipartite graph matching [HK73] we obtain a matching, i.e., a list of pairs (i_k, j_k) , s.t. $i, j = \arg\max_{i,j} M_{i,j}$. We select the $K = 3$ correspondences (i, j)

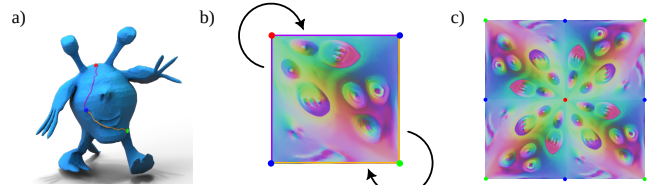


Figure 6: Seamless cuts. To parameterize a genus-zero mesh (a) we cut it open and map it to a disc topology, cut visualized as in (b). The two corresponding sides of the cut match perfectly, i.e., when we connect the two parts, thus the map remains continuous across the cut (c).

with the highest M_{ij} values, such that the geodesic distance - averaged between the two shapes - between all K points is at least $\tau = 0.3$. Finally, we use these landmarks as the two endpoints and the midpoint for the cut.

3.3.3. Seamlessness

Since we cannot rely on the quality of the cut, we reformulate the neural map h , which we optimize to define the map Ψ , to support seamlessness. This constrains the map to work on shape pairs with the same genus. Furthermore, the definition of the seamless map changes based on the genus. For a sphere, h changes to \tilde{h} :

$$\tilde{h} = \left\{ x \rightarrow T \cdot h(x) + \eta \mid T = \begin{pmatrix} a & -b \\ b & a \end{pmatrix} \in \mathbb{R}^{2 \times 2}, \eta \in \mathbb{R}^{2 \times 1} \right\} \quad (5)$$

for all points mapped outside the domain D , which rotates around the cone $c_i(\eta)$ of a rotation $R(T)$.

To achieve seamlessness h must perfectly match cones c_i to their ground truth \tilde{c}_i . Therefore, we formulate such a constraint by penalizing the deviation of mapped cones, $h(c_i)$, wrt their ground truth position:

$$\mathcal{L}_{\text{Cones}} = \|h(c_i) - \tilde{c}_i\|. \quad (6)$$

Note, independently of the genus we have 4 cones to match, one for each vertex of the square in the domain D .

A second condition for seamlessness concerns the duplicated points on the boundary. In the case of spheres, each point on the boundary p_1 has a corresponding point p_2 which is a rotation of 90° with respect to one of the cones. In the case of a torus, p_2 is on the opposite side of the boundary of p_1 , i.e., a translation. For the case of a sphere, we formulate the constraint as the following energy:

$$\mathcal{L}_{\text{Seamless}} = \|h(p_1) - R \cdot (h(p_2) - c_i) + c_i\|, \quad (7)$$

where c_i is the cones wrt p_2 undergoes a rotation R to be a clone of p_1 . Note, the rotation can either be 90° or -90° .

3.3.4. Optimization energies

We follow NSM and encourage the map to be bijective through a loss term that prevents the map h 's Jacobian J_p at every point $p \in D$ from having a negative determinant:

$$\mathcal{L}_J = \int_D \max(-\text{sign}(|J_p|)e^{-|J_p|}, 0). \quad (8)$$

Thus, encouraging continuity and bijectivity of the map. Note, due to the noisy and fuzzy nature of the correspondences obtained from a pre-trained vision transformer, we *do not guarantee* the map to be *bijective or continuous*.

To cope with the sparsity of fuzzy matches and obtain a well-defined map in undefined regions, we use an energy term that encourages smoothness and prevents extremely large amounts of distortion:

$$\mathcal{L}_{\text{Smooth}} = \int_D \|J_p^\Psi - J_{p^\varepsilon}^\Psi\|, \quad (9)$$

where J_p^Ψ is the jacobian at a point p of Ψ . While p^ε is the point p perturbed by $\varepsilon \sim \mathcal{N}(0, 0.1)$ through barycentric coordinates.

Intuitively, we want the jacobian of the map to slowly change. Note, in NSM [MAKM21], the authors used Symmetric Dirichlet [RPPSH17] in a similar context, however, this energy promotes isometric maps rather than smooth ones. Such behavior can actively damage the map optimization and force it to ignore certain - correct - matches, while we aim to attend to unregularized areas.

3.3.5. Total energy

Our total loss is expressed as:

$$\mathcal{L} = \alpha_1 \mathcal{L}_{\text{matches}} + \alpha_2 \mathcal{L}_J + \alpha_3 \mathcal{L}_{\text{Seamless}} + \alpha_4 \mathcal{L}_{\text{Cones}} + \alpha_5 \mathcal{L}_{\text{Smooth}}. \quad (10)$$

We use $\alpha_1 = 10^4$, $\alpha_2 = 10^6$, $\alpha_3 = 10^6$, $\alpha_4 = 10^6$, and $\alpha_5 = 10^{-1}$ for all experiments. We optimize network weights h using this loss, and to alleviate the impact of incorrect matches, we incrementally drop those that strongly disagree with the current map.

3.4. Rendering Settings

We render shape pairs and use these images with Dino-ViT2 [ODM*23]; this model is known to be forgiving in cases of image variation. As the shape alignment is unknown, we render an object-centric scene with a fixed perspective camera and five point lights aimed at the shape. Different points of view are obtained by rotating *only* the shape by fixed increments, while the rest of the scene (i.e., camera and lights) stays fixed. We set up the scene to ensure the entire object is visible by the field of view of the camera.

To boost the matching capabilities of Dino-ViT and aid it in distinguishing left from right, top from bottom, while enhancing scene details, we strategically position colored lights around the object in a half-dome fashion. Specifically, we employ five colored point lights (red, blue, green, yellow, and white) for this purpose. As depicted in Figure 4, corresponding regions in the images exhibit similar colors; for instance, the right part of the images tends to appear reddish due to illumination from a red light source. In cases involving textured meshes, we replace the colored lights with white ones.

4. Evaluation

We evaluated our method on various datasets for inter-surface mapping and compared it against multiple baselines that focus on obtaining surface-to-surface maps.

4.1. Datasets

We assess maps' quality on available benchmarks comprising isometric and non-isometric shape pairs. We randomly select 30 pairs from FAUST [BRLB14b], containing isometric deformations and pose variations of human shapes. We choose 30 random same-category shape pairs from SHREC07 [GBP07], containing non-isometric deformations across multiple categories of shapes. Finally, we extract 30 random shape pairs among the listed test set of SHREC19 [DSLRI9], containing a mix of isometric and non-isometric deformations.

To ablate the effect of pose variation, we use FAUST [BRLB14b], SCAPE [ASP*04], and TOSCA [BBK08]. To ablate the effects of rendering settings and rotation, we use



Figure 7: Result zoo. Automatic maps extracted by the optimization on various surface pairs using aggregated fuzzy correspondences. Colored landmarks and paths show automatically selected cones and cuts by our method.

Table 1: Quantitative evaluation. We compute each map’s accuracy (i.e., average geodesic error) and averaged them over 30 shape pairs for each dataset.

	FAUST			SHREC07			SHREC19		
	Inv ↓	Bij ↓	Acc ↓	Inv ↓	Bij ↓	Acc ↓	Inv ↓	Bij ↓	Acc ↓
ICP	0.06	0.17	0.29	0.09	0.65	0.24	0.07	0.75	0.56
BIM	0.09	0.03	0.04	0.49	0.48	0.25	0.05	0.82	0.57
Zoomout	0.33	0.23	0.73	0.25	0.65	0.55	0.29	0.76	0.59
Smooth-shells	0.01	0.00	0.01	0.03	0.72	0.23	0.01	0.83	0.57
Ours	0.00	0.00	0.07	0.00	0.00	0.26	0.00	0.00	0.55

FAUST [BRLB14b]; 3DBiCar [LCD*23], which comprise a variety of textured shapes; and SHREC15 [LZEE*15], which contain significant non-isometric-variations, with manually-annotated sparse correspondences. See supplemental for discussion.

All meshes used in our experiment are watertight and genus zero, and range from 11K to 90K faces. The shape pairs include a mix of some isometric and mostly non-isometric cases.

4.1.1. Baselines

We compare with three other techniques that focus on extracting maps between given surfaces: (i) BIM [KLF11], (ii) Zoomout [MRR*19], and (iii) Smooth-shells [ELC20]. We also include (iv) ICP, which uses the closest points as correspondence, as a strawman approach that performs well in case of negligible pose variation. Results are presented in Table 1, and depicted in Figure 9.

We cast ICP as nearest neighbor search after post-alignment. Specifically, we use our pipeline first to align each shape pair and then compute nearest neighbor matches for each point on the source to the target mesh. This approach may perform well for shapes in similar poses with low isometric deformations.

Additionally, we compare qualitatively to Enigma [EEBC20], which uses genetic algorithms along with a combinatorial search to find a set of good sparse correspondence, which are then interpolated to a dense low-distortion map. While this method produces

smoother and more semantic maps than other baselines, it still suffers from large and uneven distortions, see Figure 8.

4.2. Metrics

We assess map quality (see also [RPWO18]) based on their accuracy, bijectivity, and inversion as:

- *Accuracy* ($Acc \downarrow$): measures the ability of the algorithms to respect ground-truth correspondences. We measure it as the geodesic distance normalized, as defined in [KLF11], for each landmark.
- *Bijectivity* ($Bij \downarrow$): measures the geodesic distance of all vertices mapped forward, and then back to the source mesh wrt their original position. A zero value indicates perfect bijectivity.
- *Inversion* ($Inv \downarrow$): measures how often the map flips the surface as the percentage of inverted triangles; we compute it as the agreement of the normal of the mapped triangles wrt the faces on which the triangle vertices are mapped.

4.3. Qualitative Evaluation

Figure 7 shows Neural Semantic maps extracted using our fully automatic approach. The produced maps accurately match semantic features in spite of the fuzzy aggregated correspondences being erroneous and confused by symmetries (e.g., mapping incorrect

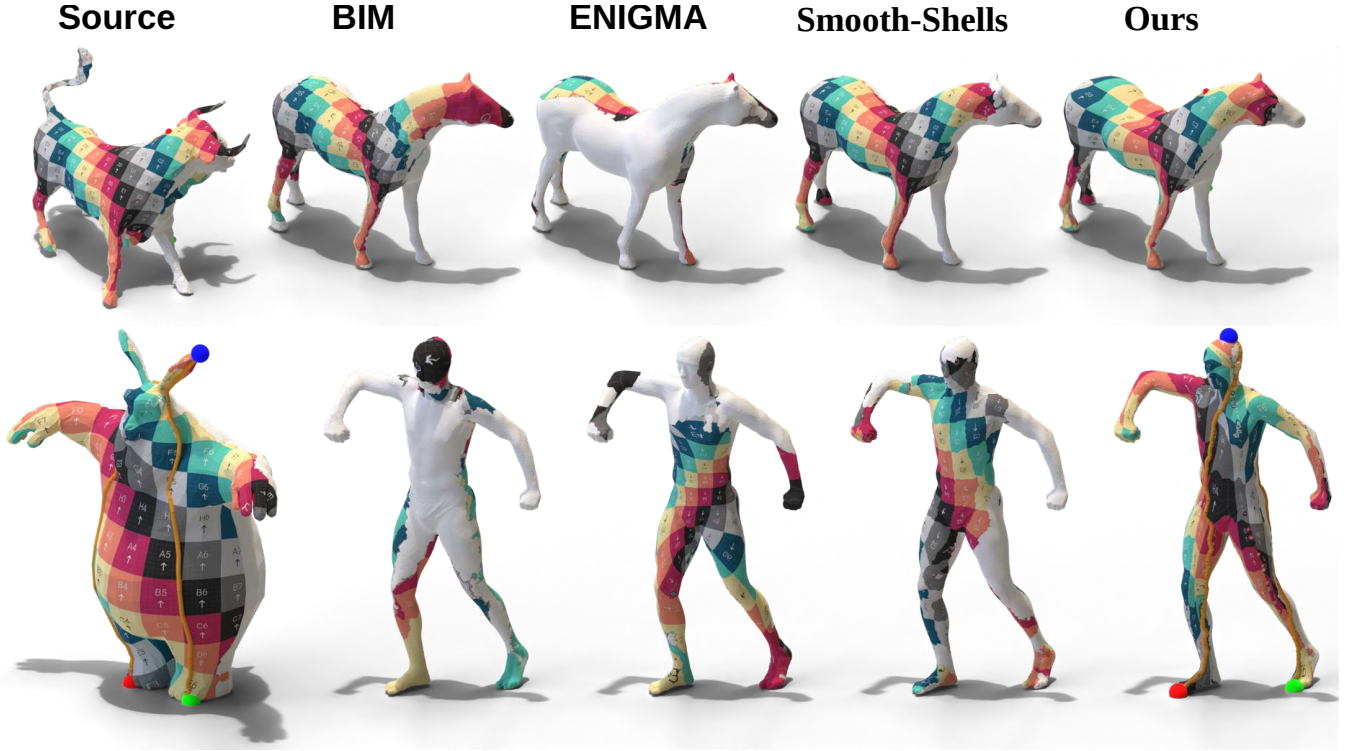


Figure 8: Qualitative comparison. ENIGMA [EEBC20] fails to produce correct mappings, in cases of extreme deformations. Similarly, other state-of-the-art methods lack bijectivity or correct correspondence. Ours can better handle these cases, see Table 1 for quantitative comparison. Colored landmarks and paths show automatically selected cones and cuts by our method.

limbs). Ours also work well across dissimilar shapes. These non-isometric cases require introducing significant local stretching, to preserve semantic correspondence. The extracted maps still exhibit low isometric distortion, where possible, while adhering to semantically meaningful correspondences. State-of-the-art methods, such as ENIGMA [EEBC19] or Smooth-shells [ELC20], suffer from self-symmetry ambiguities, e.g., see bull-horse in Figure 8.

4.4. Quantitative Evaluation

We report quantitative errors using the metrics discussed above. In particular, for accuracy, we follow the standard practice and measure the mean geodesic distance to ground truth correspondence on a unit-area mesh.

Our proposed pipeline *always* offers more bijective and continuous maps, see Table 1 "Bij" and "Inv", while others can fail to perfectly achieve these properties in both isometric and non-isometric cases. Our technique shows comparable quality in the maps compared to state-of-the-art methods, Table 1 "Acc". In general, our method suffers in isometric cases as it does not exploit geometric cues, thus producing less accurate maps than competing methods.

5. Limitations

5.1. Timing

A key limitation of our method is its long running time. The map optimization takes on average 1.5 hours, converting the meshes into their neural representation which NSM requires takes about 1 hour, and extracting all Dino-ViT matches takes 21 minutes. We plan to investigate approaches such as Meta-Learning and better caching to speed up this process.

5.2. Occlusion

The presence of self-occlusion in shape pairs prevents Dino ViT to map correctly regions between shapes, thus consistently making mistakes. We believe incorporating other priors, or an advanced rendering pipeline (e.g., layered rendering) may help cope with this issue.

5.3. Thin parts

We struggle to handle thin parts, as our pipeline requires parameterizing objects. Specifically, thin parts are difficult to handle unless cut point points are manually annotated.



Figure 9: Comparison Left-to-right: Source model, results using BIM [KLF11], ICP, Smooth-shells [ELC20], ZoomOut [MRR*19], and Ours. Although geometric methods produce good maps, they often yield discontinuous maps, e.g., see the wings of planes. Ours explicitly encourage continuity and objectivity. Colored landmarks and paths show automatically selected cones and cuts by our method. Note that Our maps are continuous across the cut seams.

6. Conclusion

We have presented a method that produces a semantic surface-to-surface map guided by visual semantic priors, by computing it from a set of candidate non-injective and discontinuous partial maps extracted by matchings over renderings of untextured 3D surfaces. Our method has many potential practical applications, ranging from matching scans of human faces and bodies to clothes, anatomical scans, and archaeological findings. These depend on the quality of the matchings achieved over the renderings of objects from these categories, which we aim to explore.

6.1. Future Work.

We require surfaces to be cut as required by NSM [MAKM21] which makes our method more prone to error. We aim to improve the existing pipeline to avoid cutting altogether by replacing the 2D disks with 3D spheres [GGS03], as successfully used in [SPK23]. Our optimization cannot guarantee to achieve a global optimum nor that the global optimum defines the “most-meaningful” semantic map, and we mark extending our method to directly *learn* to produce maps from a dataset as an important future direction. Our method can create such a dataset, augmented with manual input to score the goodness of any extracted semantic map. We believe this work is only a step in producing semantic-driven maps. Candidate fuzzy maps extracted from other means can be considered. For instance, methods to predict fuzzy geometric correspondences directly over 3D surfaces trained for specific tasks can alternatively produce fuzzy maps, and can be used in conjunction with semantic or visual cues.

Appendix A: Pseudocode

We provide pseudocode for our semantic homeomorphic map extraction framework in Algorithm 1.

Algorithm 1: Semantic Surface Homeomorphism

Data: source **A**, target **B**
 $\mathbf{R} \leftarrow \text{COALIGN}(\text{DinoViT}(), \mathbf{A}, \mathbf{B})$;
 fuzzyMatches \leftarrow
 $\text{COMPUTEMATCHES}(\text{DinoViT}(), \mathbf{A}, \mathbf{B}, \mathbf{R})$;
 $A_{\text{disk}}, B_{\text{disk}} \leftarrow \text{ASYNCCUT}(\mathbf{A}, \mathbf{B}, \text{fuzzyMatches})$;
 $A_{\text{NSM}} \leftarrow \text{OVERFITNSM}(A_{\text{disk}})$;
 $B_{\text{NSM}} \leftarrow \text{OVERFITNSM}(B_{\text{disk}})$;
 map $\leftarrow \text{DISTILMAP}(A_{\text{NSM}}, B_{\text{NSM}}, \text{fuzzyMatches})$;
 return map

Appendix B: Rendering Details

In all cases, we render images of the same size, i.e., 1344×1344 with Mitsuba using $spp = 150$ and a path integrator. When extracting semantic matches, we limit to rotations around the up-axis (y) - 20 steps between $[0, 2\pi)$ - and forward-axis (z) - 10 steps between $[-\frac{\pi}{2}, \frac{\pi}{2})$ - obtaining 200 images for each shape. Similarly, to align shapes, we rotate around the up-axis - 12 steps - with fixed increments. To uplift 2D pixels to 3D for the matches, we use ray-triangle intersection. On average, we get 328 matches per view, totaling 65k matches across the 200 views.

Appendix C: Implementation details.

We realize the neural map (h) as a 4-layer residual MLP of 128 neurons each, while neural surfaces (f) are always 8 layers residual MLP with 256 neurons. We sample 128 correspondences, 1024 points to enforce injectivity and smoothness, and 128 points for the boundary in each optimization iteration.

Appendix D: Computing rendering correspondences

As discussed in the main manuscript, we render the two surfaces from a given viewpoint to get two renderings, R_V^A and R_V^B . We leverage DinoV2 [ODM*23] to extract semantic features in the image space, thus obtaining λ_i^A and λ_i^B as features of rendering of R_V^A and R_V^B , respectively. Then, to segment foreground/background we rely on PCA first component of these features as it naturally groups them in opposite half-spaces. As the sign is appointed randomly, we use the attention mask from the last layer to select the correct half-space: we take the half-space which agrees with the average of the first PCA component associated with the positive attention mask.

Finally, we match features with the cosine similarity between all feature pairs from the same viewpoint, as score S_{ij} . We define the match of patch $i \in R_V^A$ as the patch $j \in R_V^B$ with the highest cosine similarity, and vice versa, the match of patch $j \in R_V^B$ as the patch $i \in R_V^A$ with the highest cosine similarity. In summary, the pair $(i, j), i \in R_V^A, j \in R_V^B$ is a match, if

$$S_{ij} = \max_k S_{ik} \text{ or } S_{ij} = \max_l S_{lj}. \quad (11)$$

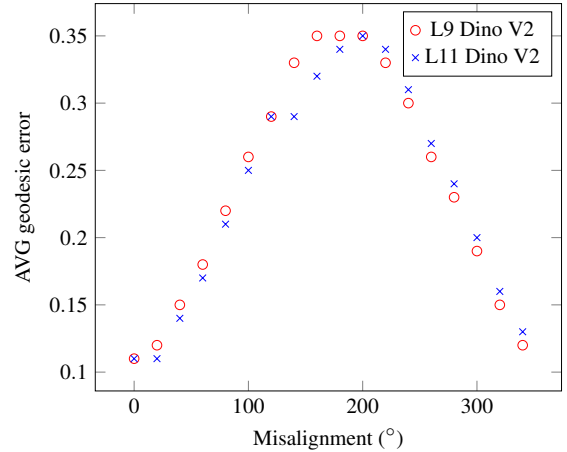


Figure 10: Robustness to misalignment: the quality of matches depends on the quality of alignment. In the case of severe misalignment (60° or more), we observe poor correspondence.

Appendix E: Comparison Details

We discuss the main considerations for/against the competing algorithms we compare against.

Blended Intrinsic Maps (BIM) [KLF11] is a classic method that uses geometric priors without any learning component. Namely,

it picks a subset of self-consistent and low-distortion conformal maps, and then blends them using weighted averages. Individual conformal maps can handle very non-isometric surfaces, however, they can produce high isometric distortion even in near-isometric cases. Note also that the resulting blended map is not a homeomorphism nor even continuous.

Zoomout [MRR*19] and Smooth-shells [ELC20] are both functional maps-based methods. Zoomout starts with a small functional correspondence matrix and iteratively upsamples it in the spectral domain. Smooth-shells follow a similar coarse-to-fine scheme, relying on shells as a proxy for functional basis. To handle self-symmetries, Eisenberger et al. [ELC20] incorporate MCMC to evaluate multiple possible functional maps.

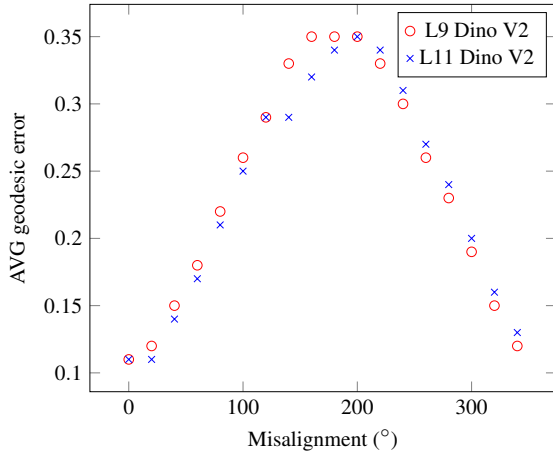


Figure 11: Robustness to misalignment: the quality of matches depends on the quality of alignment. In the case of severe misalignment (60° or more), we observe poor correspondence.

Table 2: Dino ViT pose ablation: DinoV2 [ODM*23] matches are significantly more accurate than DinoV1 [CTM*21] in case of pose variation, with no significant difference between features from L9 and L11.

Layer	FAUST		SCAPE		TOSCA	
	9	11	9	11	9	11
DinoV1	0.16	0.16	0.38	0.40	0.27	0.29
DinoV2	0.09	0.09	0.18	0.18	0.27	0.25

Table 3: Dino ViT pose ablation: DinoV2 [ODM*23] matches are significantly more accurate than DinoV1 [CTM*21] in case of pose variation, with no significant difference between features from L9 and L11.

Layer	FAUST		SCAPE		TOSCA	
	9	11	9	11	9	11
DinoV1	0.16	0.16	0.38	0.40	0.27	0.29
DinoV2	0.09	0.09	0.18	0.18	0.27	0.25

Table 4: Dino ViT ablation: DinoV2 [ODM*23] works better than its predecessor [CTM*21], with no significant difference between features from L9 and L11. The use of colored lights (rows DinoV1 and DinoV2) offers better visual cues to extract matches than white lights. Although counter-intuitive, the use of simple texture reduces the visual cues available to Dino ViT.

Layer	FAUST		SHREC15		3DBiCar	
	9	11	9	11	9	11
DinoV1	0.10	0.12	0.32	0.32	0.36	0.49
DinoV2	0.11	0.11	0.24	0.24	0.33	0.33
w/ white lights (V1)	0.20	0.18	0.27	0.35	0.38	0.38
w/ white lights (V2)	0.11	0.11	0.24	0.24	0.30	0.31
w/ texture (V1)	-	-	-	-	0.26	0.26
w/ texture (V2)	-	-	-	-	0.29	0.29

Appendix F: Ablation

Tuning DinoViT Matches

We ablate the quality of matches based on DinoViT’s degrees of freedom - layer features - in different contexts: pose variation, presence of texture, lights, and misalignment. We conduct our analysis on three distinct datasets: **FAUST** [BRLB14b], **3DBiCar** [LCD*23], and **SHREC15** [LZEE*15] each with **dense** or **sparse** ground truth.



Figure 12: Pose variation: we assess the ability of DinoV2 [ODM*23] to establish matches between shapes in different poses, as those in the figure. Experimentally, DinoV2 yields correspondences able to guide our pipeline to a proper solution. Colored landmarks and paths show automatically selected cones and cuts by our method.

Table 5: Dino ViT ablation: DinoV2 [ODM*23] works better than its predecessor [CTM*21], with no significant difference between features from L9 and L11. The use of colored lights (rows DinoV1 and DinoV2) offers better visual cues to extract matches than white lights. Although counter-intuitive, the use of simple texture reduces the visual cues available to Dino ViT.

Layer	FAUST		SHREC15		3DBiCar	
	9	11	9	11	9	11
DinoV1	0.10	0.12	0.32	0.32	0.36	0.49
DinoV2	0.11	0.11	0.24	0.24	0.33	0.33
w/ white lights (V1)	0.20	0.18	0.27	0.35	0.38	0.38
w/ white lights (V2)	0.11	0.11	0.24	0.24	0.30	0.31
w/ texture (V1)	-	-	-	-	0.26	0.26
w/ texture (V2)	-	-	-	-	0.29	0.29

We select 12 shape pairs, 4 for each dataset, to ablate texture and misalign concerning the choice of Dino ViT feature layer, as discussed in [AGBD21]. Similarly, we assess the effect of pose variation for the same model with a single instance of FAUST, SCAPE, and TOSCA mapped onto all the other provided poses. We report the quantitative results in Table 5 and show shape pairs examples and qualitative optimization results in Figure 12.

We assess the quality of the aggregated matches in terms of the normalized average geodesic distance [KLF11]. We follow the procedure described in the main paper to aggregate the fuzzy matches, thus, obtaining a face-wise map M from one mesh onto the other. Finally, the geodesic distance is computed on the target mesh between the centroid of the mapped face to the centroid of the ground truth target face.

In general, DinoV2 [ODM*23] outperforms its predecessor V1 [CTM*21], offering more accurate and robust matches. The depth at which features are extracted (9 vs 11) does not impact the matches of DinoV2, while it plays a significant role for DinoV1, as discussed in [AGBD21]. The presence of texture is beneficial to DinoV1, while it only offers a minor improvement for DinoV2. This is reassuring as our method can only assume access to untextured models. The choice of colored lights offers additional shading and visual features for DinoV1, but it is less relevant for DinoV2 as white lights perform equally with the base case.

Effect of Initial Alignment

We ablate the effect and robustness to misalignment for match quality, see Figure 11. We start from a correct alignment with 12 shape pairs and incrementally misalign one shape - step of 20° around the up axis. We report the quality of matches in terms of geodesic error, i.e., accuracy. The quality sensibly decreases with severe misalignment - more than 40° - reaching a peak with opposite orientation - 180° . We additionally compare the quality of matches for the last two layers of Dino-ViT and show that, for such a case, a deeper level (L11) seems to encode slightly better semantic information than the previous layer (L9).

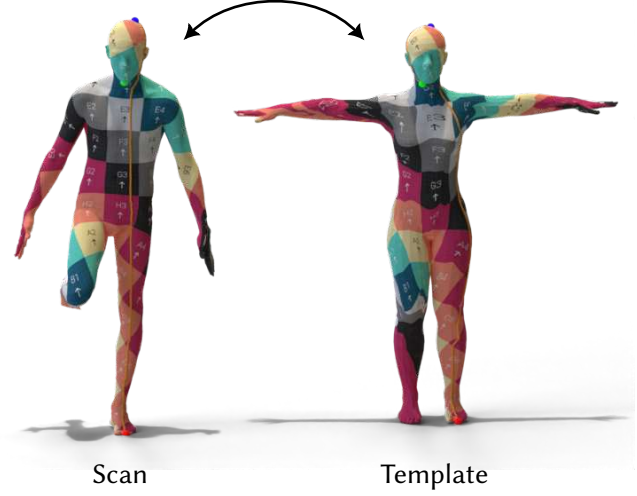


Figure 13: Scan to SMPL: we first close holes in the raw scan (left) with Meshlab, then we map it onto the template SMPL model and mask out the surfaced introduced to fill holes. Colored landmarks and paths show automatically selected cones and cuts by our method.

Handling Noise and Holes

Raw scans present noise or holes, thus inhibiting the applicability of our method since it assumes watertight genus zero meshes. Intuitively the presence of large holes, and missing limbs such as arms, may severely mislead DinoViT and thus our pipeline. On the other hand, small holes can be dealt with by applying a simple hole-filling approach. In Figure 13, we use our method to map a raw scan to the SMPL template. We prefill small holes with Meshlab and then apply our pipeline.

References

- [AEOW23] ABDELREHEEM A., ELDESKEY A., OVSJANIKOV M., WONKA P.: Zero-shot 3d shape correspondence. *arXiv preprint arXiv:2306.03253* (2023). 3
- [AGBD21] AMIR S., GANDELSMAN Y., BAGON S., DEKEL T.: Deep vit features as dense visual descriptors. *arXiv preprint arXiv:2112.05814* (2021). 2, 3, 4, 12
- [APH05] ASIRVATHAM A., PRAUN E., HOPPE H.: Consistent spherical parameterization. In *Computer Graphics and Geometric Modeling (CGMM) 2005 Workshop* (2005). 3
- [APL14] AIGERMAN N., PORANNE R., LIPMAN Y.: Lifted bijections for low distortion surface mappings. *ACM Transactions on Graphics (TOG)* 33, 4 (2014), 1–12. 3
- [APL15] AIGERMAN N., PORANNE R., LIPMAN Y.: Seamless surface mappings. *ACM Transactions on Graphics (TOG)* 34, 4 (2015), 1–13. 5
- [ASOW23] ABDELREHEEM A., SKOROKHOV I., OVSJANIKOV M., WONKA P.: Satr: Zero-shot semantic segmentation of 3d shapes. *arXiv preprint arXiv:2304.04909* (2023). 3
- [ASP*04] ANGUELOV D., SRINIVASAN P., PANG H.-C., KOLLER D., THRUN S., DAVIS J.: The correlated correspondence algorithm for unsupervised registration of nonrigid surfaces. *Advances in neural information processing systems* 17 (2004). 6

- [BBK06] BRONSTEIN A. M., BRONSTEIN M. M., KIMMEL R.: Efficient computation of isometry-invariant distances between surfaces. *SIAM J. Scientific Computing* (2006). 2
- [BBK08] BRONSTEIN A. M., BRONSTEIN M. M., KIMMEL R.: *Numerical geometry of non-rigid shapes*. Springer Science & Business Media, 2008. 6
- [BRLB14a] BOGO F., ROMERO J., LOPER M., BLACK M. J.: FAUST: Dataset and evaluation for 3D mesh registration. In *Proceedings IEEE Conf. on Computer Vision and Pattern Recognition (CVPR)* (Piscataway, NJ, USA, June 2014), IEEE. 1
- [BRLB14b] BOGO F., ROMERO J., LOPER M., BLACK M. J.: Faust: Dataset and evaluation for 3d mesh registration. In *Proceedings of the IEEE conference on computer vision and pattern recognition* (2014), pp. 3794–3801. 6, 7, 11
- [BRPM*16] BLACK M., ROMERO J., PONS-MOLL G., MAHMOOD N., BOGO F.: Learning human body shapes in motion. In *ACM SIGGRAPH 2016 Courses* (2016), SIGGRAPH '16. 1
- [BVGP09] BARAN I., VLASIC D., GRINSPOUN E., POPOVIĆ J.: Semantic deformation transfer. *ACM Trans. Graph.* 28, 3 (2009). 1
- [CAS*19] CARTER S., ARMSTRONG Z., SCHUBERT L., JOHNSON I., OLAH C.: Activation atlas. *Distill* 4, 3 (2019), e15. 3
- [CSBC*17] CORMAN E., SOLOMON J., BEN-CHEN M., GUIBAS L., OVSIANIKOV M.: Functional characterization of intrinsic and extrinsic geometry. *ACM Trans. Graph.* 36, 2 (mar 2017). URL: <https://doi.org/10.1145/2999535>, doi:10.1145/2999535. 2
- [CTM*21] CARON M., TOUVRON H., MISRA I., JÉGOU H., MAIRAL J., BOJANOWSKI P., JOULIN A.: Emerging properties in self-supervised vision transformers. In *Proceedings of the IEEE/CVF International Conference on Computer Vision* (2021), pp. 9650–9660. 3, 11, 12
- [DBI18] DENG H., BIRDAL T., ILIC S.: Ppfnet: Global context aware local features for robust 3d point matching. In *Proceedings of the IEEE conference on computer vision and pattern recognition* (2018), pp. 195–205. 2
- [DBK*20] DOSOVITSKIY A., BEYER L., KOLESNIKOV A., WEISSENBERN D., ZHAI X., UNTERTHINER T., DEGHANI M., MINDERER M., HEIGOLD G., GELLY S., ET AL.: An image is worth 16x16 words: Transformers for image recognition at scale. *arXiv preprint arXiv:2010.11929* (2020). 3
- [DLH22] DECATUR D., LANG I., HANOCKA R.: 3d highlighter: Localizing regions on 3d shapes via text descriptions. *arXiv preprint arXiv:2212.11263* (2022). 3
- [DOR*15] DEKEL T., ORON S., RUBINSTEIN M., AVIDAN S., FREEMAN W. T.: Best-buddies similarity for robust template matching. In *Proceedings of the IEEE conference on computer vision and pattern recognition* (2015), pp. 2021–2029. 4
- [DSL19] DYKE R., STRIDE C., LAI Y., ROSIN P.: Shrec-19: shape correspondence with isometric and non-isometric deformations. 6
- [DSO20] DONATI N., SHARMA A., OVSIANIKOV M.: Deep geometric functional maps: Robust feature learning for shape correspondence. In *Proceedings of the IEEE/CVF Conference on Computer Vision and Pattern Recognition* (2020), pp. 8592–8601. 2
- [EBC17] EZUZ D., BEN-CHEN M.: Deblurring and denoising of maps between shapes. In *Symposium on Geometry Processing* (2017). 3
- [EEBC19] EDELSTEIN M., EZUZ D., BEN-CHEN M.: Enigma: evolutionary non-isometric geometry matching. *arXiv preprint arXiv:1905.10763* (2019). 8
- [EEBC20] EDELSTEIN M., EZUZ D., BEN-CHEN M.: Enigma: Evolutionary non-isometric geometry matching. In *ACM Transactions on Graphics* (2020). 3, 7, 8
- [ELC20] EISENBERGER M., LAHNER Z., CREMERS D.: Smooth shells: Multi-scale shape registration with functional maps. In *Proceedings of the IEEE/CVF Conference on Computer Vision and Pattern Recognition* (2020), pp. 12265–12274. 7, 8, 9, 11
- [EST*19] EGGER B., SMITH W. A. P., TEWARI A., WUHRER S., ZOLLHÖFER M., BEELER T., BERNARD F., BOKART T., KORTYLEWSKI A., ROMDHANI S., THEOBALT C., BLANZ V., VETTER T.: 3d morphable face models - past, present and future. *CoRR abs/1909.01815* (2019). URL: <http://arxiv.org/abs/1909.01815>. 2
- [GBP07] GIORGI D., BIASOTTI S., PARABOSCHI L.: Shrec: shape retrieval contest: Watertight models track. *Online*: <http://watertight.gemati.cnr.it> 7 (2007). 6
- [GDDM14] GIRSHICK R., DONAHUE J., DARRELL T., MALIK J.: Rich feature hierarchies for accurate object detection and semantic segmentation. In *Proceedings of the IEEE conference on computer vision and pattern recognition* (2014), pp. 580–587. 3
- [GEB16] GATYS L. A., ECKER A. S., BETHGE M.: Image style transfer using convolutional neural networks. In *Proceedings of the IEEE conference on computer vision and pattern recognition* (2016), pp. 2414–2423. 3
- [GGS03] GOTSMAN C., GU X., SHEFFER A.: Fundamentals of spherical parameterization for 3d meshes. *ACM Trans. Graph.* 22, 3 (jul 2003), 358–363. 10
- [GYK*21] GENOVA K., YIN X., KUNDU A., PANTOFARU C., COLE F., SUD A., BREWINGTON B., SHUCKER B., FUNKHOUSER T.: Learning 3d semantic segmentation with only 2d image supervision. *3DV* (2021). 3
- [GZWW19] GOJCIC Z., ZHOU C., WEGNER J. D., WIESER A.: The perfect match: 3d point cloud matching with smoothed densities. In *Proceedings of the IEEE/CVF Conference on Computer Vision and Pattern Recognition* (2019), pp. 5545–5554. 2
- [HAWG08] HUANG Q.-X., ADAMS B., WICKE M., GUIBAS L. J.: Non-Rigid Registration Under Isometric Deformations. *Computer Graphics Forum* (2008). doi:10.1111/j.1467-8659.2008.01285.x. 2
- [HDT19] HU W., DANG A., TAN Y.: A survey of state-of-the-art short text matching algorithms. In *International Conference on Data Mining and Big Data* (2019). 1
- [HK73] HOPCROFT J. E., KARP R. M.: An $n^5/2$ algorithm for maximum matchings in bipartite graphs. *SIAM Journal on computing* 2, 4 (1973), 225–231. 5
- [HKC*17] HUANG H., KALOGERAKIS E., CHAUDHURI S., CEYLAN D., KIM V. G., YUMER E.: Learning local shape descriptors from part correspondences with multiview convolutional networks. *ACM Transactions on Graphics* 37, 1 (2017). 3
- [HWAG09] HUANG Q., WICKE M., ADAMS B., GUIBAS L.: Shape decomposition using modal analysis. In *Computer Graphics Forum (Proceedings of Eurographics 2009)* (Munich, Germany, April 2009), vol. 28, pp. 407–416. doi:10.1111/j.1467-8659.2009.01380.x. 2
- [HZH*22] HAMILTON M., ZHANG Z., HARIHARAN B., SNAVELY N., FREEMAN W. T.: Unsupervised semantic segmentation by distilling feature correspondences. *arXiv preprint arXiv:2203.08414* (2022). 2, 3
- [KAMC17] KALOGERAKIS E., AVERKIOU M., MAJI S., CHAUDHURI S.: 3D shape segmentation with projective convolutional networks. In *Proc. IEEE Computer Vision and Pattern Recognition (CVPR)* (2017). 3
- [KLF11] KIM V. G., LIPMAN Y., FUNKHOUSER T.: Blended intrinsic maps. *Transactions on Graphics (Proc. of SIGGRAPH)* 30, 4 (2011). 3, 7, 9, 10, 12
- [KMR*23] KIRILLOV A., MINTUN E., RAVI N., MAO H., ROLLAND C., GUSTAFSON L., XIAO T., WHITEHEAD S., BERG A. C., LO W.-Y., ET AL.: Segment anything. *arXiv preprint arXiv:2304.02643* (2023). 3
- [KYF*20] KUNDU A., YIN X., FATHI A., ROSS D., BREWINGTON B., FUNKHOUSER T., PANTOFARU C.: Virtual multi-view fusion for 3d semantic segmentation. *ECCV* (2020). 3

- [LCD*23] LUO Z., CAI S., DONG J., MING R., QIU L., ZHAN X., HAN X.: Rabbit: Parametric modeling of 3d biped cartoon characters with a topological-consistent dataset. *arXiv preprint arXiv:2303.12564* (2023). 7, 11
- [LLSH23] LI J., LI D., SAVARESE S., HOI S.: Blip-2: Bootstrapping language-image pre-training with frozen image encoders and large language models. *arXiv preprint arXiv:2301.12597* (2023). 3
- [LLUZ16] LUO W., LI Y., URTASUN R., ZEMEL R.: Understanding the effective receptive field in deep convolutional neural networks. *Advances in neural information processing systems* 29 (2016). 3
- [LRB*18] LITANY O., RODOLA E., BRONSTEIN A., BRONSTEIN M., CREMERS D.: Partial single-and multishape dense correspondence using functional maps. *Handbook of Numerical Analysis* (2018). 2
- [LRR*17] LITANY O., REMEZ T., RODOLA E., BRONSTEIN A., BRONSTEIN M.: Deep functional maps: Structured prediction for dense shape correspondence. In *Proceedings of the IEEE international conference on computer vision* (2017), pp. 5659–5667. 2
- [LZEE*15] LIAN Z., ZHANG Z., EL ELMAGHY H., EL SANA J., FURUYA T., GIACHETTI A., GÜLER A., LAI L., LI C., LI H., ET AL.: Shrec 15 track non rigid 3d shape retrieval. 7, 11
- [MAKM21] MORREALE L., AIGERMAN N., KIM V. G., MITRA N. J.: Neural surface maps. In *Proceedings of the IEEE/CVF Conference on Computer Vision and Pattern Recognition* (2021), pp. 4639–4648. 2, 3, 5, 6, 10
- [MCA*22] MURALIKRISHNAN S., CHAUDHURI S., AIGERMAN N., KIM V., FISHER M., MITRA N.: Glass: Geometric latent augmentation for shape spaces. In *Proceedings of the IEEE/CVF Conference on Computer Vision and Pattern Recognition* (2022). 2
- [MGY*19] MO K., GUERRERO P., YI L., SU H., WONKA P., MITRA N., GUIBAS L.: Structurenet: Hierarchical graph networks for 3d shape generation. *arXiv preprint arXiv:1908.00575* (2019). 3
- [MJF*21] MA J., JIANG X., FAN A., JIANG J., YAN J.: Image matching from handcrafted to deep features: A survey. *Int. J. Comput. Vision* 129, 1 (2021), 23–79. 1
- [MRR*19] MELZI S., REN J., RODOLA E., SHARMA A., WONKA P., OVSJANIKOV M.: Zoomout: Spectral upsampling for efficient shape correspondence. *arXiv preprint arXiv:1904.07865* (2019). 7, 9, 11
- [OBSC*12] OVSJANIKOV M., BEN-CHEN M., SOLOMON J., BUTSCHER A., GUIBAS L.: Functional maps: a flexible representation of maps between shapes. *ACM Transactions on Graphics (ToG)* 31, 4 (2012), 1–11. 2
- [OCB*17] OVSJANIKOV M., CORMAN E., BRONSTEIN M., RODOLA E., BEN-CHEN M., GUIBAS L., CHAZAL F., BRONSTEIN A.: Computing and processing correspondences with functional maps. *SIGGRAPH Course Notes* (2017). 3
- [ODM*23] OQUAB M., DARCET T., MOUTAKANNI T., VO H., SZAFRANIEC M., KHALIDOV V., FERNANDEZ P., HAZIZA D., MASSA F., EL-NOUBY A., ET AL.: Dinov2: Learning robust visual features without supervision. *arXiv preprint arXiv:2304.07193* (2023). 2, 3, 4, 6, 10, 11, 12
- [OMS17] OLAH C., MORDVINTSEV A., SCHUBERT L.: Feature visualization. *Distill* 2, 11 (2017), e7. 3
- [PRM*21] PAI G., REN J., MELZI S., WONKA P., OVSJANIKOV M.: Fast sinkhorn filters: Using matrix scaling for non-rigid shape correspondence with functional maps. In *Proceedings of the IEEE/CVF Conference on Computer Vision and Pattern Recognition* (2021), pp. 384–393. 3
- [PWH*15] PISHCHULIN L., WUHRER S., HELTEN T., THEOBALT C., SCHIELE B.: Building statistical shape spaces for 3d human modeling. *CoRR abs/1503.05860* (2015). URL: <http://arxiv.org/abs/1503.05860>. 1
- [RL01] RUSINKIEWICZ S., LEVOY M.: Efficient variants of the icp algorithm. In *Proceedings third international conference on 3-D digital imaging and modeling* (2001), IEEE, pp. 145–152. 2
- [RMOW20] REN J., MELZI S., OVSJANIKOV M., WONKA P.: Maptree: recovering multiple solutions in the space of maps. *ACM Trans. Graph.* 39, 6 (2020), 264–1. 3
- [RPPSH17] RABINOVICH M., PORANNE R., PANOZZO D., SORKINE-HORNUNG O.: Scalable locally injective mappings. *ACM Transactions on Graphics (TOG)* 36, 4 (2017), 1. 5, 6
- [RPWO18] REN J., POULENARD A., WONKA P., OVSJANIKOV M.: Continuous and orientation-preserving correspondences via functional maps. *ACM Transactions on Graphics (ToG)* 37, 6 (2018), 1–16. 3, 7
- [Sah20] SAHILIOĞLU Y.: Recent advances in shape correspondence. *The Visual Computer* 36, 8 (2020), 1705–1721. 2
- [SAPH04] SCHREINER J., ASIRVATHAM A., PRAUN E., HOPPE H.: Inter-surface mapping. In *ACM SIGGRAPH 2004 Papers*. 2004, pp. 870–877. 3
- [SBCK19] SCHMIDT P., BORN J., CAMPEN M., KOBBELT L.: Distortion-minimizing injective maps between surfaces. *ACM Transactions on Graphics (TOG)* 38, 6 (2019), 1–15. 3
- [SGM*20] SHOCHER A., GANDELSMAN Y., MOSSERI I., YAROM M., IRANI M., FREEMAN W. T., DEKEL T.: Semantic pyramid for image generation. In *Proc. CVPR* (2020), pp. 7457–7466. 3
- [SMKL15] SU H., MAJI S., KALOGERAKIS E., LEARNED-MILLER E. G.: Multi-view convolutional neural networks for 3d shape recognition. In *Proc. ICCV* (2015). 3
- [SP04] SUMNER R. W., POPOVIĆ J.: Deformation transfer for triangle meshes. *ACM Trans. Graph.* 23, 3 (aug 2004), 399–405. 1
- [SPK23] SCHMIDT P., PIEPER D., KOBBELT L.: Surface Maps via Adaptive Triangulations. *Computer Graphics Forum* (2023). doi: 10.1111/cgf.14747. 3, 10
- [SPKS16] SOLOMON J., PEYRÉ G., KIM V. G., SRA S.: Entropic metric alignment for correspondence problems. *ACM Transactions on Graphics (ToG)* 35, 4 (2016), 1–13. 2
- [SPV*21] SIMÉONI O., PUY G., VO H. V., ROBURIAN S., GIDARIS S., BURSUC A., PÉREZ P., MARLET R., PONCE J.: Localizing objects with self-supervised transformers and no labels. *arXiv preprint arXiv:2109.14279* (2021). 2, 3
- [SYM*22] SHARMA G., YIN K., MAJI S., KALOGERAKIS E., LITANY O., FIDLER S.: Mvdecor: Multi-view dense correspondence learning for fine-grained 3d segmentation. In *ECCV* (2022). 3
- [SZF20] SUN H., ZHOU W., FEI M.: A survey on graph matching in computer vision. In *Intn. Congress on Image and Signal Processing, BioMedical Engineering and Informatics (CISP-BMEI)* (2020), pp. 225–230. 1
- [TP91] TURK M., PENTLAND A.: Eigenfaces for Recognition. *Journal of Cognitive Neuroscience* 3, 1 (01 1991), 71–86. 1
- [VHVZ22] VAZE S., HAN K., VEDALDI A., ZISSERMAN A.: Generalized category discovery. In *Proceedings of the IEEE/CVF Conference on Computer Vision and Pattern Recognition* (2022), pp. 7492–7501. 2, 3
- [WGGH18] WANG X., GIRSHICK R., GUPTA A., HE K.: Non-local neural networks. In *Proceedings of the IEEE conference on computer vision and pattern recognition* (2018), pp. 7794–7803. 3
- [WS19] WANG Y., SOLOMON J. M.: Deep closest point: Learning representations for point cloud registration. In *Proceedings of the IEEE/CVF International Conference on Computer Vision* (2019), pp. 3523–3532. 2
- [WSH*22] WANG Y., SHEN X., HU S. X., YUAN Y., CROWLEY J. L., VAUFREYDAZ D.: Self-supervised transformers for unsupervised object discovery using normalized cut. In *Proceedings of the IEEE/CVF Conference on Computer Vision and Pattern Recognition* (2022), pp. 14543–14553. 3
- [YYPM11] YANG Y.-L., YANG Y.-J., POTTMANN H., MITRA N. J.: Shape space exploration of constrained meshes. *ACM Transactions on Graphics* 30, 6 (2011). 2

- [ZLW*20] ZHU H., LUO M., WANG R., ZHENG A., HE R.: Deep audio-visual learning: A survey, 2020. URL: <https://arxiv.org/abs/2001.04758>, doi:10.48550/ARXIV.2001.04758. 1
- [ZSN03] ZINSSER T., SCHMIDT J., NIEMANN H.: A refined icp algorithm for robust 3-d correspondence estimation. In *Proceedings 2003 international conference on image processing (Cat. No. 03CH37429)* (2003), vol. 2, IEEE, pp. II–695. 2